RESEARCH ARTICLE

NANO · MICRO small
www.small-journal.com

# An All-in-One Array of Pressure Sensors and sEMG Electrodes for Scoliosis Monitoring

*Weizhe Fan, Shenglong Wang, Qingyang Li, Xiarong Ren, Chengcheng Zhang, Hanyue Wang, Murong Li, Weiqing Yang, and Weili Deng**

**Scoliosis often occurs in adolescents and seriously affects physical development and health. Traditionally, medical imaging is the most common means of evaluating the corrective effect of bracing during treatment. However, the imaging approach falls short in providing real-time feedback, and the optimal corrective force remains unclear, potentially slowing the patient's recovery progress. To tackle these challenges, an all-in-one integrated array of pressure sensors and sEMG electrodes based on hierarchical MXene/chitosan/polydimethylsiloxane (PDMS)/polyurethane sponge and MXene/polyimide (PI) is developed. Benefiting from the microstructured electrodes and the modulus enhancement of PDMS, the sensor demonstrates a high sensitivity of 444.3 $kPa^{-1}$ and a broad linear detection range (up to 81.6 kPa). With the help of electrostatic attraction of chitosan and interface locking of PDMS, the pressure sensor achieves remarkable stability of over 100 000 cycles. Simultaneously, the sEMG electrodes offer exceptional stretchability and flexibility, functioning effectively at 60% strain, which ensures precise signal capture for various human motions. After integrating the developed all-in-one arrays into a commercial scoliosis brace, the system can accurately categorize human motion and predict Cobb angles aided by deep learning. This study provides real-time insights into brace effectiveness and patient progress, offering new ideas for improving the efficiency of scoliosis treatment.**

## 1. Introduction

Scoliosis is a medical condition characterized by a lateral curve of the human spine, forming an "S" or "C" shape. Scoliosis can be categorized as idiopathic or secondary according to its etiology,[1] both of which can pose a significant threat to patients' health if not treated properly.[2] The Cobb angle is widely recognized as the predominant metric for quantifying scoliosis and is crucial in guiding treatment decisions.[3,4] Usually, surgical treatment is needed for patients with a Cobb angle over 45°, whereas patients with a Cobb angle in the 20°–40° range can be treated with bracing.[5,6] The brace gradually restores the spine to its normal state by applying corrective force to the abnormal curvature. X-ray imaging is the primary means of judging the effectiveness of brace therapy.[7,8] Throughout brace treatment, on average, each scoliosis patient receives 10–25 spinal X-ray examinations periodically, with a radiation dose reaching 10–25 mGy.[9] This method of imaging evaluation is not only radiation-intensive and medically expensive, but also cannot provide timely feedback on the effectiveness of the correction. Therefore, the study of real-time detection of the therapeutic effect of traditional braces is of great significance for the treatment of scoliosis.

Monitoring the corrective force exerted by the brace, in addition to X-ray imaging, can offer an alternative method for evaluating the efficiency of brace correction. In normal conditions, the interface pressure exerted by the brace ranges from 37.6 to 80.6 kPa,[10] characterized by rapid change and long duration. Consequently, pressure sensors for brace monitoring must have a wide detection range, high sensitivity, and exceptional stability. Furthermore, wearing comfort should also be considered since the brace can be worn for 18–23 hours per day,[11] requiring a high degree of flexibility in the sensor. Advancements in sensing technologies have elevated the role of flexible sensors in wearable devices and personalized medicine,[12–20] offering a noninvasive alternative for tracking scoliosis progression. Among them, the piezoresistive 3D conductive sponges, whose resistance varies with external pressure or stimuli, have emerged as a favored material for flexible and

W. Fan, S. Wang, Q. Li, X. Ren, C. Zhang, H. Wang, M. Li, W. Yang, W. Deng
Key Laboratory of Advanced Technologies of Materials (Ministry of Education)
School of Materials Science and Engineering
Southwest Jiaotong University
Chengdu, Sichuan 610031, P. R. China
E-mail: weili1812@swjtu.edu.cn

S. Wang
School of Chemistry
Southwest Jiaotong University
Chengdu, Sichuan 610031, P. R. China

W. Yang
Research Institute of Frontier Science
Southwest Jiaotong University
Chengdu, Sichuan 610031, P. R. China

The ORCID identification number(s) for the author(s) of this article can be found under https://doi.org/10.1002/smll.202404136

DOI: 10.1002/smll.202404136

 

wearable pressure sensors due to their outstanding performance, straightforward fabrication, and easy circuit integration.[21–25] Sponge-based piezoresistive sensors have been reported in various forms, including different conductive materials, device structures, and multiple applications, such as human motion monitoring or human–machine interfaces.[26–33] However, most of the current research tends to improve the sensitivity of the sensors at the expense of the operating range, thus making it difficult to meet the monitoring requirements of scoliosis braces. In addition to pressure sensors, surface electromyography (sEMG) plays a significant role in scoliosis treatment.[34–36] Research has shown that the root mean square (RMS) ratio of bilateral paravertebral muscles is relevant to the Cobb angle.[37,38] Since the sEMG electrodes are in direct contact with human skin and the patient is engaged in varying activities, the electrodes must possess a certain degree of stretchability to ensure a tight fit, and thus signal fidelity.

Here, we design an all-in-one array of pressure sensors and sEMG electrodes for scoliosis braces that combines brace pressure detection with myoelectric signal analysis to evaluate the corrective effects. By introducing polydimethylsiloxane (PDMS) into the MXene/chitosan-based polyurethane (PU) sponge (PCMP), the resultant pressure sensor exhibits a sensitivity of 444.3 $kPa^{-1}$ and a linear detection range of up to 81.6 kPa, with high stability over 100 000 compression cycles. Benefiting from the serpentine structure, the obtained sEMG electrodes exhibit decent stretchability. With the assistance of a machine learning algorithm, the smart brace, which integrates an array of pressure sensors and sEMG electrodes, can indicate the motion status of the patient and provide information about the Cobb angle. This work is expected to be a new way to monitor scoliosis brace treatment in real time.

## 2. Results and Discussion

### 2.1. Design of Flexible Pressure Sensors and sEMG Electrodes

Accurate signal acquisition and analysis in scoliosis treatment rely heavily on high-performance pressure sensors and sEMG electrodes. As illustrated in **Figure 1a**, the pressure sensors and the sEMG electrodes are integrated into a single unit. Among them, the chitosan/PDMS double-interface locked effect and the microstructure ensure the accuracy and long-term stability of the pressure sensing. On the other hand, inspired by the cellular structure of human skin, the sEMG electrodes are designed with a dense serpentine network that mimics the intercellular tension filaments between cells, which enables the electrodes to achieve excellent stretchability in various sensing circumstances.

After integrating the pressure sensors and sEMG electrodes, the final array is schematically shown in Figure 1b. Then, the integrated array is deployed inside the scoliosis brace to form the dorsal domain network (Figure 1c). Scoliosis affects the spine in multiple ways, manifesting symptoms such as thoracic compression and pelvic tilt (Figure 1d).[39,40] The paraspinal muscles are considered to be strongly associated with scoliosis progression, so monitoring the sEMG of bilateral paravertebral muscles (Figure 1e) may be valuable in predicting the progression of idiopathic scoliosis.[34] Meanwhile, the paravertebral muscles of the curved spine produce different tension patterns and muscular imbalances (Figure 1f) during asymmetric movement,[36] which can reflect the pressure distribution of the brace. Therefore, we can enhance the understanding and real-time detection of scoliosis progression by analyzing the collected sEMG and pressure signals from scoliosis braces wearers (Figure 1g).

### 2.2. Fabrication and Characterization of PCMP and sEMG Electrodes

The micropillar-structured electrode for the pressure sensor is prepared by laser engraving on a polyimide (PI) film. As shown in **Figure 2a**, the prepared pillar-like structure exhibits a uniform distribution, which is favorable for enhancing the performance of piezoresistive sensors by increasing the whole electrode surface area while reducing the initial contact area. MXene, known for its superior electrical properties and high modifiability, is emerging as a highly promising material for pressure sensors.[41] For the preparation of MXene ($Ti_3C_2T_x$) nanosheets, Al in the precursor $Ti_3AlC_2$ was first etched with LiF and HCl via the minimally intensive layer delamination method,[28] followed by an ultrasonic fragmentation process (Figure S1, Supporting Information). From the TEM image (Figure 2b), it can be seen that the MXene nanosheets extend laterally to several hundred nanometers and possess a hexagonal crystal structure with a thickness of about a few nanometers (Figure 2c). The lightweight and large deformation capability of the PU sponge make it an ideal for scoliosis brace as a pressure-sensing substrate material. To enhance the binding of MXene with the sponge, the PU sponge is first modified with chitosan, which utilizes the large difference in surface charge between MXene and chitosan to allow for better adsorption of MXene onto the sponge. As can be seen in Figure S2 (Supporting Information), the zeta potential of MXene is −11.1 mV, whereas chitosan is 0.4 mV. After the adsorption of MXene by chitosan, the MXene nanosheets are then wrapped around the sponge skeleton with a PDMS layer to form a double-interface lock with a PU-chitosan-MXene-PDMS structure. Figure 2d shows the photo of PCMP (10 cm × 10 cm) fabricated by a dip-drying process, and its internal structure is shown in Figures 2e,f. The energy-dispersive X-ray spectroscopy (EDS) element mapping shows the homogenous distribution of Ti, Si, and C over the PCMP (Figure 2g). The FTIR spectra of the sequentially fabricated PU sponge reveal distinct chemical signatures corresponding to each fabrication step, demonstrating the successful addition of chitosan, MXene, and PDMS (Figure 2h). In detail, pure MXene exhibits characteristic peaks at 3448 and 1627 $cm^{-1}$, attributed to the O—H stretching vibrations of surface hydroxyl groups and the C═O stretching vibrations from surface carbonyl functionalities, respectively. Chitosan shows a C—H stretching vibration at 2874 $cm^{-1}$ and a C═O stretching vibration at 1651 $cm^{-1}$, indicating the presence of carbonyl groups. The PU spectrum is characterized by a broad C—H stretching region from 2841 to 3004 $cm^{-1}$, a complex C═O stretching region from 1621 to 1742 $cm^{-1}$ indicative of various carbonyl functionalities within the urethane linkages, a C═C stretching vibration at 1537 $cm^{-1}$, and a C—O stretching vibration at 1092 $cm^{-1}$, reflecting its ether linkages. Upon dipping PU in chitosan, the retention of characteristic PU and chitosan peaks suggests a physical coating rather than a chemical interaction since there are

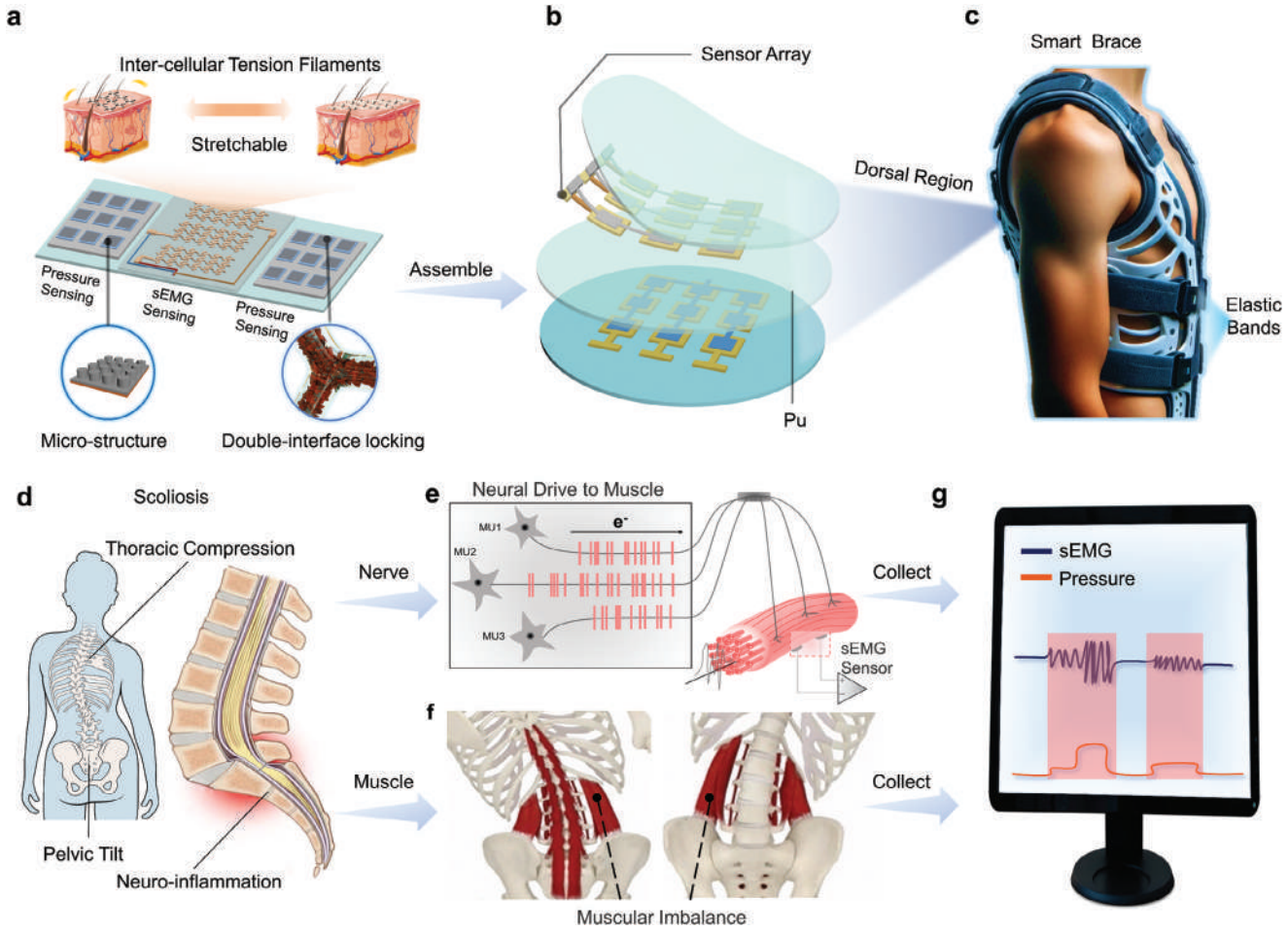


**Figure 1.** Schematic illustration of pressure sensor and sEMG electrodes for scoliosis monitoring. a) All-in-one array of pressure sensors and sEMG electrodes. Top: skin cellular structure inspiration of sEMG electrodes. Bottom: microstructure electrodes and double-interface locked effect of pressure sensors. b) Array of pressure sensors and sEMG electrodes for scoliosis brace. c) Brace integrated with pressure sensors/sEMG electrodes array on the wearer. d) Symptoms of scoliosis. e) sEMG reflection of scoliosis. f) Muscular imbalance in scoliosis patients. g) Pressure/sEMG signal joint detection for scoliosis patients.

no new or significant shifts in the existing peaks. Meanwhile, adding MXene to the PU-chitosan complex does not significantly alter the spectral profile. The final encapsulation with PDMS is evidenced by the emergence of distinct peaks at 1260 and 1024 $cm^{-1}$, attributed to $–CH_3$ and Si—O stretching vibrations, respectively. On this basis, the water vapor transmission rate (WVTR) test reveals that PCMP has a WVTP of 266.28 g $m^{-2}$ $d^{-1}$, which is lower than pure PU sponge and chitosan/MXene dipped sponge (CMP), meaning that the addition of PDMS occupies some inner space of the sponge and hints the role of PDMS altering the modulus of the pure sponge. In the meantime, compared to pure PDMS film, PCMP offers improved permeability, which is suitable for the moist conditions within a scoliosis brace due to sweat evaporation (Figure 2i). Also, PCMP exhibits a larger water contact angle (WCA) of 138° compared to pure PU sponge (110°), chitosan dipped sponge (CP) (124°) and CMP (114°) (Figure 2j), which further demonstrates its suitability for in-brace application under sweaty conditions. The compression tests of PCMP samples show that immersion in PDMS improved the compressive strength of the devices. As the degree of cross-linking of PDMS increases, the compressive strength reaches 331.2 kPa (Figure S3, Supporting Information), significantly greater than that of pure PU sponge (45.8 kPa). However, too high compression modulus/strength may cause foreign body sensation, so PDMS with an A:B ratio of 4 (compressive strength of 253 kPa) is chosen for subsequent experiments. Figure 2k illustrates the stress–strain curves for the selected PCMP at maximum compressive strains of 10%, 20%, 40%, 60%, and 80%. The behavior of PCMP can be divided into three distinct deformation zones: the elastic zone (minor strain: $\varepsilon < 5\%$), the plateau zone (intermediate strain: $5\% < \varepsilon < 50\%$), and the densification zone (high strain: $\varepsilon > 50\%$). In the elastic zone, stress rises linearly, primarily due to the deformation of the sponge structure. During the plateau zone, the stress gradually increases and tends to stabilize, resulting from the enhanced skeletal contact within the PCMP. In the densification zone, further compression causes a steep increase in stress due to the formation of additional skeletal contacts within the sponge, resulting in the densification region. Besides, a cyclic compression test (100 cycles) was conducted to evaluate the mechanical stability of PCMP. The resulting cyclic stress–strain

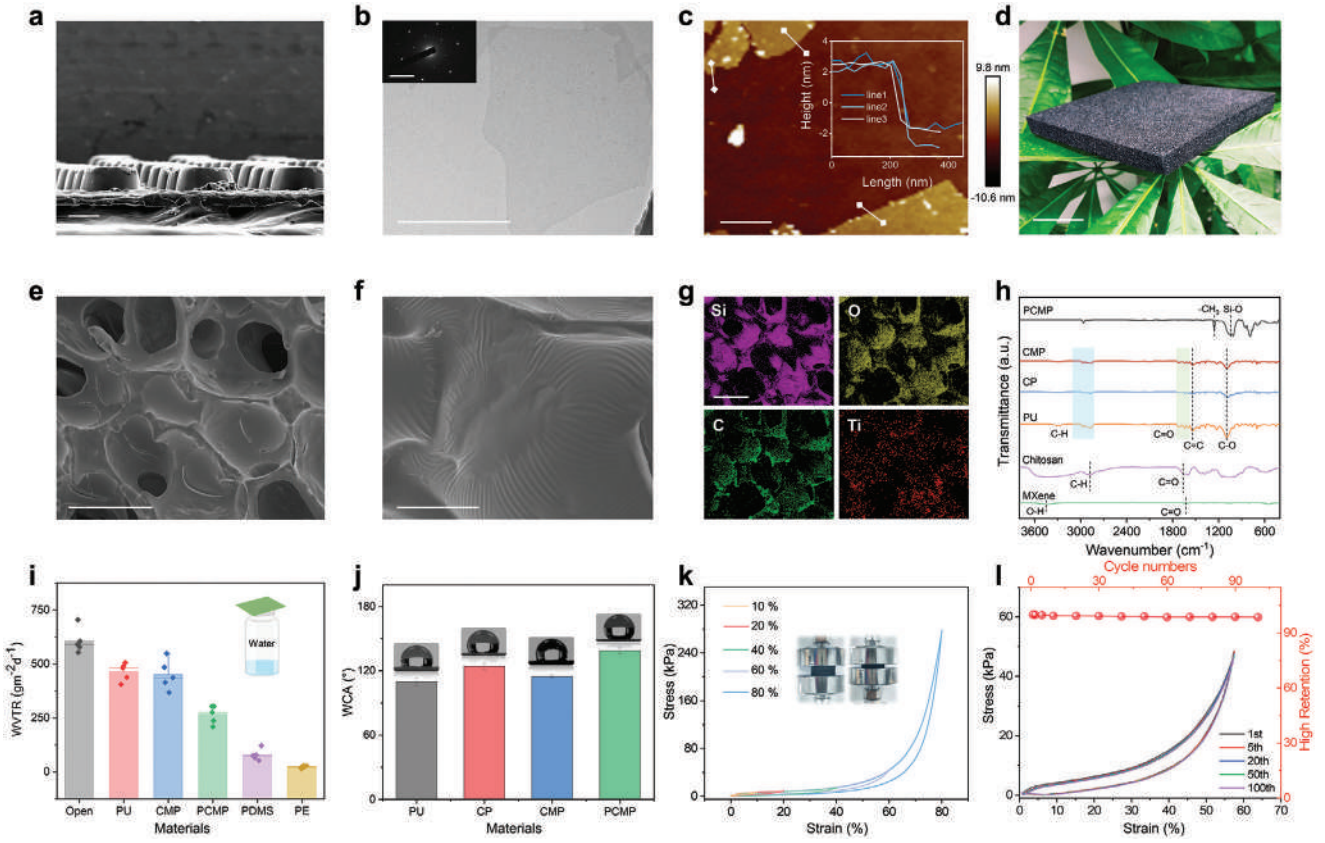


**Figure 2.** Fabrication and characterization of PCMP device. a) SEM image of the micropillar-structured electrode. Scale bar, 100 µm. b) TEM image and corresponding Selected Area Electron Diffraction (SAED) pattern (inset) of individual MXene nanosheets. Scale bar, 500 nm (5 1/nm inset). c) AFM image of MXene nanosheets. Scale bar, 500 nm. d) Photograph of the large-sized PCMP. Scale bar, 2 cm. e,f) SEM images showing the internal structure of PCMP sensitive layer. Scale bar, 500 µm (e), 100 µm (f). g) The corresponding elemental maps of Si, O, C, and Ti. Scale bar, 500 µm. h) FTIR spectra of MXene, chitosan, PU, CP, CMP, and PCMP. i) Water vapor transmission rate test of different materials. j) Water contact angle of PU, CP, CMP, and PCMP. k) Results of compression tests of PCMP sensor under different strains. l) Compression cycle characterization of PCMP sensor.

curves (Figure 2l) generally overlap and exhibit narrow hysteresis loops, indicating excellent mechanical stability and small energy dissipation during the compress–release process.

### 2.3. Sensing Performance and Mechanism of PCMP Device

Due to the sensitive layer being bolstered by a cylindrical microstructured electrode, the designed PCMP exhibits exceptional pressure sensing performance under different static pressures, with a consistent rise in relative current change (**Figure 3a**). The device's current–voltage ($I$–$V$) characteristics indicate a solid ohmic contact, suggesting charge transport efficiency (Figure S4a, Supporting Information). A range of concentrations of MXene (0.5, 1, and 2 mg mL$^{-1}$) were used in the sponge material to study the sensing performance of the PCMP sensor. The result shows that the sensitivity of PCMP with 1 mg mL$^{-1}$ MXene can achieve 444.3 kPa$^{-1}$ over a wide pressure range of 0–81.6 kPa with a coefficient of determination ($R^2$) of 0.998 (Figure 3b), which is crucial for force monitoring in scoliosis braces. In addition, the PCMP shows a rapid response/recovery time of 45/25 ms, which is sufficient to respond accurately to stimuli with different frequencies (0.2–1 Hz), as demonstrated in Figure 3c and Figure S4b in the Supporting Information. To elucidate the PCMP sensor's mechanism, we constructed a three-stage visual model, as shown schematically in Figure 3d. In the initial stage, without any pressure, there is little contact between the microstructure and the sensitive layer, and there are almost no conductive paths. When a low pressure is applied in the second state, the microstructure comes into contact with the sensitive layer, decreasing device resistance. In the third stage, when a higher pressure is applied, the sensitive layer of PCMP deforms and the space between MXene nanosheets decreases, resulting in new conductive paths that lead to a significant decrease in device resistance, which is manifested as an increase in conductivity. Besides, the contact areas between the sensitive layer and microstructure electrodes increase simultaneously under high pressure, further enhancing the current by lowering the interface resistance. This mechanism allows the PCMP device to surpass conventional 3D material-based (sponge, aerogel, foam) sensors that often compromise between high sensitivity and wide detection range (Figure 3e; Table S1, Supporting Information).[27–33,42–45] Superior stability is achieved by adding chitosan and PDMS to enhance the attachment of MXene onto the sponge skeleton. Figure 3f depicts how MXene nanosheets are locked in a PCMP device and detached from the

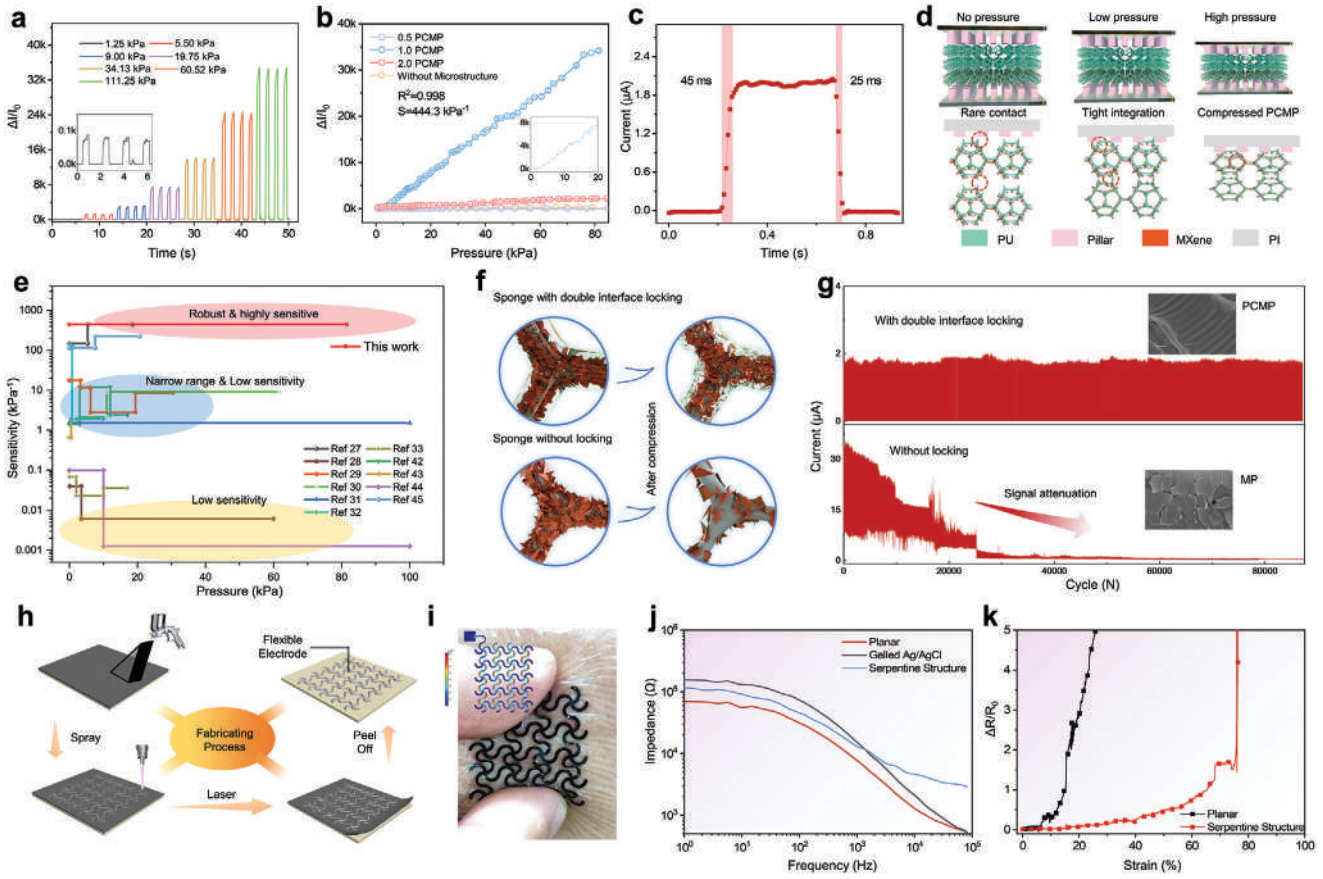


**Figure 3.** Illustration of the sensing performance and mechanism of the PCMP sensor. a) Relative current response of a PCMP sensor under various pressures. b) Pressure sensitivities of the PCMP sensor with different MXene nanosheet concentrations. c) Response and recovery time of PCMP sensor. d) Working mechanism of the PCMP sensor in three stages. e) Comparison of the sensitivity and detection range between PCMP sensor and other 3D materials (Sponge, Aerogel, Foam) based pressure sensors. f) Illustration of the double-interface locked effect. g) Current response of the PCMP sensor and MP over 100 000 compression-release cycles, the embedded SEM images show the situation of MXene nanosheets attachment to sponge skeleton after cycles. Scale bar, 10 μm. h) Fabrication process of serpentine-structure sEMG electrodes. i) sEMG electrode contact with human skin under squeeze and FEA result of the strain distribution of sEMG electrodes under tension condition (inset). j) Contact impedance of planar electrode, gelled Ag/AgCl, and serpentine-structure electrode. k) Relative resistance changes of planar and serpentine-structure electrodes in tension tests.

skeleton. Repeated compression/release cycle tests show no signal degradation for the PCMP, whereas the degradation for the MXene dipped sponge (MP) is pronounced (Figure 3g), demonstrating the remarkable robustness of the PCMP sensor. After the cycle tests, the SEM images (Figure 3g inset) show no shedding of MXene in PCMP and significant shedding in MP, further confirming the advantage of the double-interface locked effect. The fabrication process of bionic sEMG electrodes comprises MXene layer spray, laser cutting of serpentine structure and peeling off, as depicted in Figure 3h. Finite element analysis (FEA) under compression (Figure 3i) demonstrates the electrode's high mechanical stability. Benefiting from the firm bond of PU tape, the electrodes maintain close contact with the skin even under compression, ensuring high-quality signal acquisition (Figure 3i). Figure 3j compares the contact impedance of three different electrodes (commercial gelled Ag/AgCl electrode, MXene planar electrode, and MXene serpentine electrode), where the serpentine electrodes fall between the commercial Ag/AgCl electrode and the MXene planar electrode, exhibiting relatively low contact impedance within the sEMG spectrum (below 450 Hz).[46] Nonetheless, the change in resistance of the serpentine electrodes under tension is small compared to the MXene planar electrode (Figure 2k). Even under 60% strain, the small resistance change allows serpentine electrodes to function properly, which further demonstrates their reliability in collecting signals during human movements.

### 2.4. Machine Learning-Based Motion Classification and Cobb Angle Prediction

Monitoring the scoliosis brace is crucial during treatment, offering personalized insights into physiological changes. A volunteer donned a commercial scoliosis brace with an all-in-one array consisting of a 10×10 pressure sensor array and six sEMG electrodes attached to the paravertebral muscles bilaterally (**Figure** 4a). The pressure sensor array consists of top and bottom electrodes, a sensing layer, an insulating layer, and a polyimide encapsulation layer (Figure 4b; Figure S5, Supporting Information). Figure 4c presents a diagram for data acquisition, signal preprocessing,

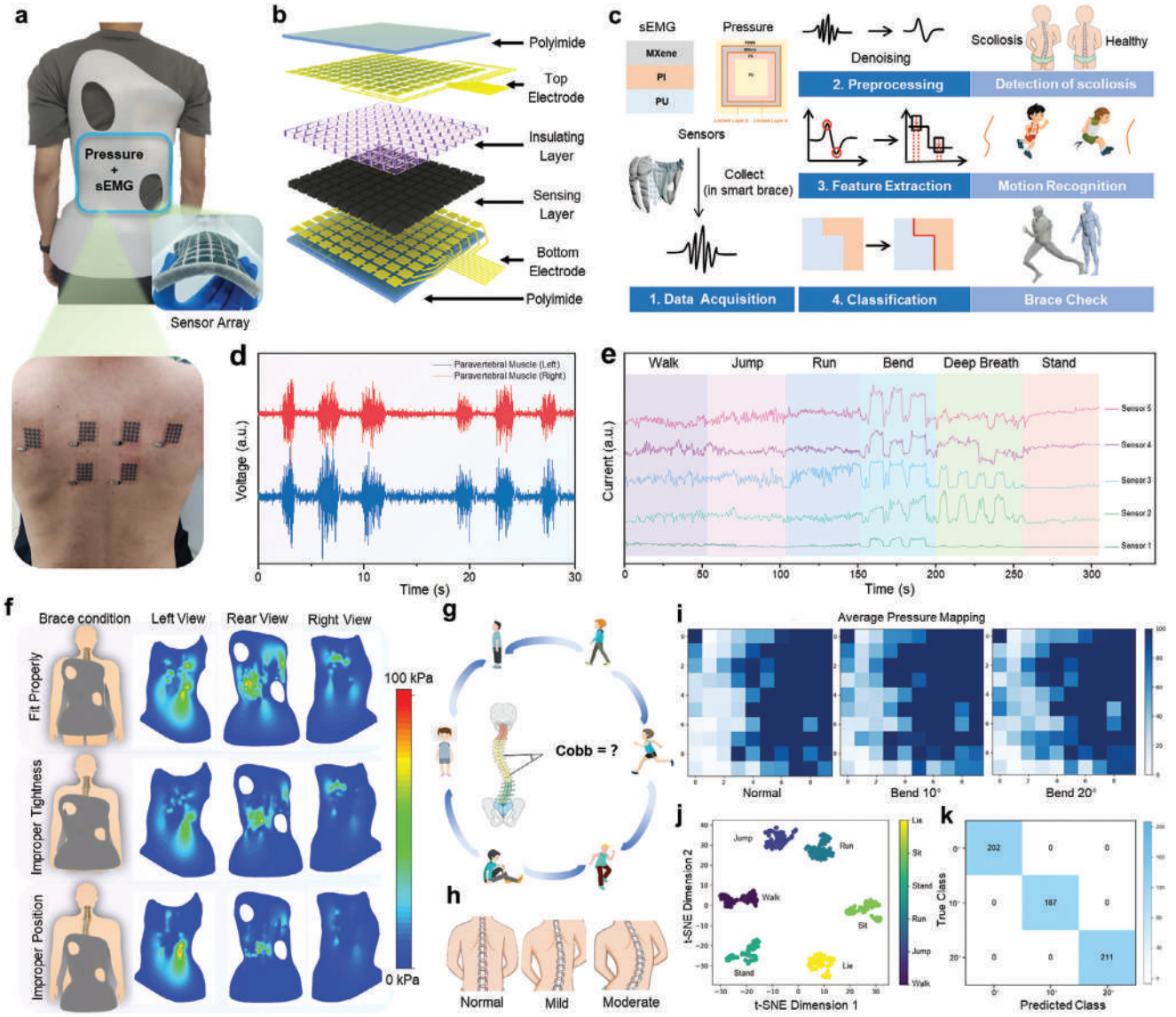


**Figure 4.** A machine learning-assisted system for in-brace pressure and sEMG signal analysis. a) Illustration of the volunteer wearing a commercial brace integrated with pressure sensors and sEMG electrodes. b) Assembly of the pressure sensor array. c) Workflow diagram of the whole system. d) sEMG signals of bilateral paravertebral muscles during strengthening. e) Pressure signals of multiple motions. f) Pressure distribution map of three brace states g) Illustration of predicting different motions and Cobb angle h) Schematic of three spinal statuses. i) Pressure distribution map of three different spinal states. j) Visualizing the output data after machine learning adopting t-distributed stochastic neighbor embedding (t-SNE) dimensionality reduction. k) Confusion matrix for three different spinal states.

feature extraction, and classification designed for the PCMP sensors and the serpentine sEMG electrodes. The volunteer performed back-strengthening exercises to capture pressure and sEMG signals (Figure 4d). According to the correlation between the RMS in sEMG and the Cobb angle, the curvature of the spine can be predicted by the sEMG signals of the bilateral paravertebral muscles.[37,38] Figure 4e displays signals from five typical pressure sensors in the array during various actions, indicating distinctive patterns for six different movements, forming the basis for motion and Cobb angle recognition through machine learning. When the brace was worn by the volunteer in different states, including correct wear, improper tightness, and incorrect position, the pressure distribution of the brace was mapped in Figure 4f. As a result, it could be used to remind the wearers to adjust braces to achieve a better correction. On this basis, different 2D convolutional neural networks (CNN) were designed to identify the movement patterns and predict the Cobb angle of scoliosis patients (Figures 4g,h). When volunteers wear a brace equipped with PCMP sensors for different activities, the proposed CNN model achieves high classification accuracy in lying, sitting, standing, running, jumping, and walking after 50 training epochs (Figure S6a, Supporting Information). The confusion matrix shows no erroneous judgment in predicting six motions, demonstrating the feasibility of a CNN-assisted pressure sensor array for human motion recognition (Figure S6b, Supporting Information). The low-dimension t-SNE

visualization (Figure 4j) depicts the six motions in six colored clusters transformed from the high-dimensional input pressure data, further confirming the superiority in data acquisition of the developed PCMP sensor. By statistically averaging the pressure data over a certain time frame, the average pressure map was drawn to show different pressure distribution patterns for spine with normal, bending 10° and bending 20° states (Figure 4i). With the help of machine learning, Cobb angle classification prediction can be achieved by analyzing the data collected by the sensing array (Figure 4k). The developed all-in-one sensing array combined with machine learning algorithms enables real-time monitoring of scoliosis, which provides a reference for the visualization of brace treatment and improving treatment efficiency.

## 3. Conclusion

In summary, we developed an all-in-one sensing array with high-performance pressure sensors and bio-inspired serpentine sEMG electrodes using conductive MXene nanosheets to provide patients with a radiation-free means of scoliosis evaluation. Benefiting from the chitosan/PDMS double-interface locked effect, the PCMP pressure sensor achieved a high sensitivity of 444.3 $kPa^{-1}$ and a broad linear detection range of up to 81.6 kPa, as well as a superb stability over 100 000 compression/release cycles. Meanwhile, the flexible sEMG electrodes attained an accurate signal acquisition due to the low contact impedance. With the assistance of neural networks, it was preliminarily verified that the developed all-in-one sensing array could recognize human motions and the Cobb angle in scoliosis. Combined with clinical data, the smart brace integrated with an all-in-one array of PCMP sensors and sEMG electrodes can hopefully become a noninvasive and radiation-free device for scoliosis brace treatment.

## 4. Experimental Section

*Preparation of MXene Nanosheets*: MXene ($Ti_3C_2T_X$) was synthesized by selectively etching aluminum (Al) in $Ti_3AlC_2$ (Jilin 11 Company) (Figure S7a, Supporting Information). In detail, 2 g of LiF was added into 40 mL HCl (9 M) and stirred for 15 min. Then, $Ti_3AlC_2$ (2 g, 400 mesh size) was mixed with the solution and undergone stirring for 24 h at 40 °C. After that, the acidic suspension was washed with deionized water until pH > 6. The product of $Ti_3C_2T_X$ was dispersed in DI water by ultrasonication for 1.5 h. In the end, the supernatant containing $Ti_3C_2T_X$ nanosheets was collected after centrifugation at 3500 rpm for 1 h.[47]

*Fabrication of PCMP Device*: The PU sponge was first dipped in a chitosan solution (0.2 mg $mL^{-1}$) for 1 h, and dried at 80 °C for 1 h to obtain CP.[48] Then, the CP was dipped in MXene solution for 1 h (the concentration is controlled by the ratio of MXene nanosheets and deionized water), followed by drying at 80 °C for 1 h to obtain CMP. PCMP was finally obtained by dipping CMP in PDMS/ n-Hexane solution for 1 h, and undergone 1 h drying at 80 °C. The microstructure electrodes were fabricated by laser marking the PI film to engrave micropillars on the surface, combined with a magnetron sputtering process to plate with Ag. At the end, the PCMP layer and microstructure electrodes were encapsulated with an ultrathin polyurethane tape (Figure S7b, Supporting Information), resulting in a dimension of 11 cm × 11 cm × 1 cm.

*Fabrication of sEMG Electrodes*: The PI film was first treated with oxygen plasma (15 min) to improve its hydrophilicity (Figure S8, Supporting Information), thus enhancing its adhesion to MXene nanosheets. A spray gun was used to spray the preprepared MXene supernatant onto the treated PI film. Then, a serpentine structure was carved out using a laser-engraving machine. Finally, the sEMG electrodes were obtained by peeling off the excess part, resulting in a dimension of 3.9 cm × 3.8 cm × 150 μm.

*Characterization and Measurement*: The characterization of the samples was performed through scanning electron microscopy (SEM, JSM-7800) with an accelerating voltage of 5 kV. The morphology of MXene nanosheets was obtained by transmission electron microscopy (JEM 2100F). The FTIR (Thermo Fisher Nicolet Is10) spectra were applied to study the composition of MXene, chitosan, PDMS and PCMP. To evaluate the pressure sensing performance, a linear motor equipped with a force sensor was utilized to apply pressure to the device and the corresponding current signals were measured by a low-noise current sensitive preamplifier (Stanford, SR570). The *I–V* curves were measured by an electrochemical workstation (CH Instruments, CHI660E). Human pressure and sEMG data were collected primarily to validate the feasibility of the sensing array in monitoring human motion and scoliosis. The volunteer is a healthy person who wears a scoliosis brace that is customized for a scoliosis sufferer. All testing from human participants was approved by the Institutional Review Boards of Southwest Jiaotong University with the reference number of SWJTU23012-NSFC(133). The informed consent was obtained from all volunteers before enrollment in this study.

*Convolutional Neural Networks (CNN) for Human Motion Classification and Cobb Angle Recognition*: Two CNN models were developed in Python based on Keras and Tensorflow. The pressure data was collected through an Arduino microcontroller based on the pressure sensor array. The first model was applied to extract data features and classify human motion. The total datasets were 600 and the dimension of each dataset inputted into CNN was 10 × 10. Among all the datasets, 80% were allocated as training sets and the rest were test sets. The accuracy and loss function of training and testing processes were evaluated to showcase the model performance. The second model was compiled using the Adam optimizer and categorical cross-entropy loss function for training. The dataset was divided into three sets of training data, each containing 10 samples, totaling 3000 samples using data augmentation techniques to expand the dataset to enhance the model's generalization capability. Among the datasets, 80% were designated for training, while the remainder served as test sets. The accuracy and loss functions of both training and testing phases were assessed to demonstrate the model's performance.

*Statistical Analysis*: All the experiments were conducted in triplicate. The obtained data were expressed as the mean value ± standard deviation. Data processing was performed using Origin software.

## Supporting Information

Supporting Information is available from the Wiley Online Library or from the author.

## Acknowledgements

W.F., S.W. and Q.L. contributed equally to this work. This research was financially supported by the Fundamental Research Funds for the Central Universities (No. 202210613065), the Natural Science Foundation of Sichuan Province of China (No. 2023NSFSC0313) and the Basic Research Cultivation Project of Southwest Jiaotong University (No. 2682023KJ024). Thanks for the help from the Analysis and Testing Center of Southwest Jiaotong University.

## Conflict of Interest

The authors declare no conflict of interest.

## Data Availability Statement

The data that support the findings of this study are available from the corresponding author upon reasonable request.

## Keywords

brace, cobb angle, pressure sensor, scoliosis monitoring, sEMG electrode

Received: May 22, 2024
Revised: July 26, 2024
Published online:

[1] S. Haleem, C. Nnadi, *Paediatr. Child Health* **2018**, *28*, 209.
[2] G. Ruiz, N. J. Torres-Lugo, P. Marrero-Ortiz, H. Guzman, G. Olivella, N. Ramirez, *EFORT Open Rev.* **2022**, *7*, 599.
[3] S. Langensiepen, O. Semler, R. Sobottke, O. Fricke, J. Franklin, E. Schönau, P. Eysel, *Eur. Spine J.* **2013**, *22*, 2360.
[4] J. Cobb, *Instr. Course Lect.* **1948**, *5*, 261.
[5] T. Maruyama, K. Takeshita, *Clin. Med. Insights: Pediatr.* **2009**, *3*, S2117.
[6] F. Zaina, C. Cordani, S. Donzelli, S. G. Lazzarini, C. Arienti, M. J. Del Furia, S. Negrini, *Children (Basel)* **2022**, *9*, 1672.
[7] P. Knott, E. Pappo, M. Cameron, J. C. deMauroy, C. Rivard, T. Kotwicki, F. Zaina, J. Wynne, L. Stikeleather, J. Bettany-Saltikov, *Scoliosis Growth, Proc. Symp., 3rd* **2014**, *9*, 4.
[8] T. Kotwicki, *Disabil. Rehabil.: Assist. Technol.* **2008**, *30*, 742.
[9] P. A. Oakley, N. N. Ehsani, D. E. Harrison, *Dose Response* **2019**, *17*, 1559325819852810.
[10] A. Ahmad, N. A. Abu Osman, H. Mokhtar, W. Mehmood, N. A. Kadri, *Proc. Inst. Mech. Eng., Part H* **2019**, *233*, 901.
[11] M. R. Konieczny, P. Hieronymus, R. Krauspe, *Spine J.* **2017**, *17*, 1658.
[12] W. Deng, Y. Zhou, A. Libanori, G. Chen, W. Yang, J. Chen, *Chem. Soc. Rev.* **2022**, *51*, 3380.
[13] J. Yin, S. Wang, T. Tat, J. Chen, *Nat. Rev. Bioeng.* **2024**, *2*, 541.
[14] Z. Shi, L. Meng, X. Shi, H. Li, J. Zhang, Q. Sun, X. Liu, J. Chen, S. Liu, *Nano-Micro Lett.* **2022**, *14*, 141.
[15] J. Li, Q. Ding, H. Wang, Z. Wu, X. Gui, C. Li, N. Hu, K. Tao, J. Wu, *Nano-Micro Lett.* **2023**, *15*, 105.
[16] J. Liu, G. Tian, W. Yang, W. Deng, *Soft Sci.* **2022**, *2*, 22.
[17] K. Liu, M. Wang, C. Huang, Y. Yuan, Y. Ning, L. Zhang, P. Wan, *Adv. Sci.* **2024**, *11*, 2305672.
[18] Y. Zhang, Z. Xu, X. Chu, M. Li, Y. Yuan, W. Wang, L. Zhang, P. Wan, *Device* **2024**, *2*, 100253.
[19] G. Tian, W. Deng, T. Yang, J. Zhang, T. Xu, D. Xiong, B. Lan, S. Wang, Y. Sun, Y. Ao, *Adv. Mater.* **2024**, *36*, 2313612.
[20] S. Wang, Y. Yao, W. Deng, X. Chu, T. Yang, G. Tian, Y. Ao, Y. Sun, B. Lan, X. Ren, *ACS Nano* **2024**, *18*, 11183.
[21] X. Zang, X. Wang, Z. Yang, X. Wang, R. Li, J. Chen, J. Ji, M. Xue, *Nanoscale* **2017**, *9*, 19346.
[22] X. Dong, Y. Wei, S. Chen, Y. Lin, L. Liu, J. Li, *Compos. Sci. Technol.* **2018**, *155*, 108.
[23] L. Lv, P. Zhang, T. Xu, L. Qu, *ACS Appl. Mater. Interfaces* **2017**, *9*, 22885.
[24] L. Qiu, Y. Tang, J. Liu, T. Alan, J. Ding, V. Truong, D. Li, *Adv. Mater.* **2015**, *28*, 194.
[25] Y. Ding, T. Xu, O. Onyilagha, H. Fong, Z. Zhu, *ACS Appl. Mater. Interfaces* **2019**, *11*, 6685.
[26] X. Ren, S. Wang, D. Xiong, G. Tian, B. Lan, W. Yang, W. Deng, *Chem. Eng. J.* **2024**, *485*, 149817.
[27] Y. Yue, N. Liu, W. Liu, M. Li, Y. Ma, C. Luo, S. Wang, J. Rao, X. Hu, J. Su, *Nano Energy* **2018**, *50*, 79.
[28] X. Wang, Y. Tao, S. Pan, X. Fang, C. Lou, Y. Xu, J. Wu, M. Sang, L. Lu, X. Gong, T. Luo, S. Xuan, *npj Flexible Electron.* **2022**, *6*, 95.
[29] W. Cao, Y. Luo, Y. Dai, X. Wang, K. Wu, H. Lin, K. Rui, J. Zhu, *ACS Appl. Mater. Interfaces* **2023**, *15*, 3131.
[30] H. Zhang, N. Liu, Y. Shi, W. Liu, Y. Yue, S. Wang, Y. Ma, L. Wen, L. Li, F. Long, Z. Zou, Y. Gao, *ACS Appl. Mater. Interfaces* **2016**, *8*, 22374.
[31] Q. Wei, G. Chen, H. Pan, Z. Ye, C. Au, C. Chen, X. Zhao, Y. Zhou, X. Xiao, H. Tai, Y. Jiang, G. Xie, Y. Su, J. Chen, *Small Methods* **2022**, *6*, 2101051.
[32] T. Chen, X. Zhang, X. Hu, Z. Wu, F. Cao, X. A. Wang, B. Wu, X. Fang, Y. Xie, *Chem. Eng. J.* **2020**, *401*, 126029.
[33] X. Wu, Y. Han, X. Zhang, Z. Zhou, C. Lu, *Adv. Funct. Mater.* **2016**, *26*, 6246.
[34] J. Cheung, J. P. Halbertsma, A. G. Veldhuizen, W. J. Sluiter, N. M. Maurits, J. C. Cool, J. R. van Horn, *Eur. Spine J.* **2005**, *14*, 130.
[35] M. Reuber, A. Schultz, T. Mcneill, D. Spencer, *Spine* **1983**, *8*, 447.
[36] W. Chwała, A. Koziana, T. Kasperczyk, R. Walaszek, M. Płaszewski, *Biomed Res. Int.* **2014**, *2014*, 573276.
[37] V. Feipel, C.-E. Aubin, O. Ciolofan, M. Beauséjour, H. Labelle, P. Mathieu, *Med. Biol. Eng. Comput.* **2002**, *40*, 497.
[38] W. Yuan, L. Chen, J. Shen, H. Wang, K. Yu, Y. Liu, J. Zhou, Y. Lin, *J. Tissue Eng.* **2019**, *23*, 3824.
[39] J. L. Huec, A. Cogniet, S. Mazas, A. Faundez, *Eur. J. Orthop. Surg. Traumatol.* **2016**, *26*, 705.
[40] A. Ploumis, E. E. Transfledt, F. Denis, *Spine J.* **2007**, *7*, 428.
[41] D. Lei, N. Liu, T. Su, Q. Zhang, L. Wang, Z. Ren, Y. Gao, *Adv. Mater.* **2022**, *34*, 2110608.
[42] J. Li, N. Li, Y. Zheng, D. Lou, Y. Jiang, J. Jiang, Q. Xu, J. Yang, Y. Sun, C. Pan, *Adv. Sci.* **2022**, *9*, 2201912.
[43] M. Cao, S. Fan, H. Qiu, D. Su, L. Li, J. Su, *ACS Appl. Mater. Interfaces* **2020**, *12*, 36540.
[44] H. Guo, Y. J. Tan, G. Chen, Z. Wang, G. J. Susanto, H. H. See, Z. Yang, Z. W. Lim, L. Yang, B. C. Tee, *Nat. Commun.* **2020**, *11*, 5747.
[45] L. Li, Y. Cheng, H. Cao, Z. Liang, Z. Liu, S. Yan, L. Li, S. Jia, J. Wang, Y. Gao, *Nano Energy* **2022**, *95*, 106986.
[46] R. Merletti, P. Di Torino, *J. Electromyogr. Kinesiol.* **1999**, *9*, 3.
[47] S. Wang, W. Deng, T. Yang, Y. Ao, H. Zhang, G. Tian, L. Deng, H. Huang, J. Huang, B. Lan, W. Yang, *Adv. Funct. Mater.* **2023**, *33*, 2214503.
[48] X. P. Li, Y. Li, X. Li, D. Song, P. Min, C. Hu, H. B. Zhang, N. Koratkar, Z. Z. Yu, *J. Colloid Interface Sci.* **2019**, *542*, 54.